A Dual-Band Wireless Power Transfer and Backscatter Communication Approach for Real-Time Neural/EMG Data Acquisition

Eleftherios Kampianakis, *Student Member, IEEE*, Apoorva Sharma, *Student Member, IEEE*, José Arenas, and Matthew S. Reynolds, *Senior Member, IEEE*

***Abstract*—We present a dual-band approach for HF wireless power delivery and UHF backscatter communication in implanted biomedical devices. A testbed is described including a custom implant device as well as an external system based around the USRP B210 software defined radio platform. The implant integrates a binary phase shift keying backscatter uplink rate of 5 Mb/s, with an HF wireless power transfer link delivering 1.33 mW at an efficiency of 17%. The implant is 25 mm in diameter and 2.8 mm thick, including the printed circuit substrate, dual-band antenna, all circuitry, and biocompatible silicone encapsulation. It supports up to ten neural and four electromyogram (EMG) channels with a sampling rate of 26.10 kHz for the neural channels and 1.628 kHz for the EMG channels. The communication link is shown to have 0% packet error rate at an implant depth of up to 2.5 cm.**

***Index Terms*—Biomedical devices, implanted devices, backscatter communication, wireless power transfer, dual band.**

I. Introduction

IMPLANTABLE neuroprosthetic devices are an area of increasing research interest due to the large number of clinical indications that neuroprosthetics could address. These clinical indications include muscle spasticity and pain [1], seizures, dystonia, severe depression and many others [2]. As a result, numerous research and industry teams are working to implement a new class of bioelectronic devices incorporating amplification, digitization and wireless transmission of neural activity, along with electrical and/or optogenetic stimulation of neurons. Despite promising early results, significant electronic, electromagnetic, thermal, and packaging challenges remain to be solved [3], [4].

Supporting a high channel count of neural inputs is critical for research in neuroprosthetic and brain-computer interface (BCI) applications [5], [6]. However, the number of channels that a system can telemeter to an external system is ultimately constrained by its communication rate. High bandwidth conventional wireless systems (such as IEEE 802.11 / WiFi) using active transmitters consume tens to hundreds of milliwatts and are therefore thermally unfavorable for implanted applications where power dissipation into tissue is limited to the order of 10 mW/cm^3. Since low power dissipation is a critical constraint for implanted systems, various non-traditional communication modalities have been explored. A few examples in the literature include radio frequency (RF) modulated backscatter [3], [7]–[9], backscatter of ultrasound [10], and impulse radio ultrawideband (IR-UWB) transmission [11].

In addition to the aforementioned communication challenges, efficient power delivery is also a significant issue, especially in chronic (long-term) implanted devices where battery exchange is undesirable. Wireless power transfer (WPT) using magnetic induction has been widely used for this purpose; many prior systems (including [12] and [13]) have shown high efficiency inductive WPT in the 13.56 MHz industrial, scientific and medical (ISM) band.

An alternative WPT approach relies on near-field coupling of UHF energy; an integrated BCI system including both near-field UHF WPT and backscatter communication is described in [3] and [14]. This work presents a 64-channel implantable neural recording system using the UHF band for both wireless power and backscatter communication. However, this system is limited to 1 Mbps communication rate and thus its sampling rate is confined to only 1 kHz per channel.

This work aims to combine high speed UHF modulated backscatter communication with efficient HF WPT in a single implantable system. The system is a combination of a custom implant device, with a commercial low-cost software defined radio (SDR) platform serving as the external system. A block diagram of this system is shown in Fig. 1. The implanted device is powered by a 13.56 MHz WPT link, and uplinks neural recording data at 915 Mhz using a binary phase shift keying (BPSK) backscatter modulator. The external SDR supplies a continuous wave (CW) carrier at 915 MHz and downconverts the backscattered signal to provide a host PC with baseband I/Q samples for software demodulation using GNUradio and MATLAB. An external self-jammer cancellation network suppresses the reflected carrier energy to greatly improve receiver sensitivity. To the best of our knowledge, this is the first demonstration of a complete backscatter-based implantable

Manuscript received June 29, 2017; accepted August 21, 2017. Date of publication August 25, 2017; date of current version November 30, 2017. This work was supported by the National Science Foundation under Award EEC-1028725. *(Corresponding author: Eleftherios Kampianakis.)*

E. Kampianakis, A. Sharma, and J. Arenas are with the Department of Electrical Engineering, University of Washington, Seattle, WA 98195 USA (e-mail: ekampian@uw.edu).

M. S. Reynolds is with the Department of Electrical Engineering, University of Washington, Seattle, WA 98195 USA, and also with the Paul G. Allen School of Computer Science and Engineering, University of Washington, Seattle, WA 98195 USA.

Digital Object Identifier 10.1109/JRFID.2017.2745460

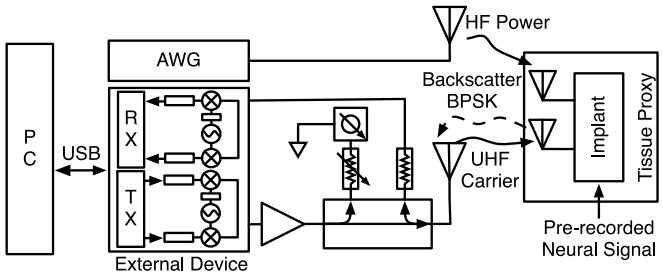

Fig. 1. High-rate implantable communication system testbed.

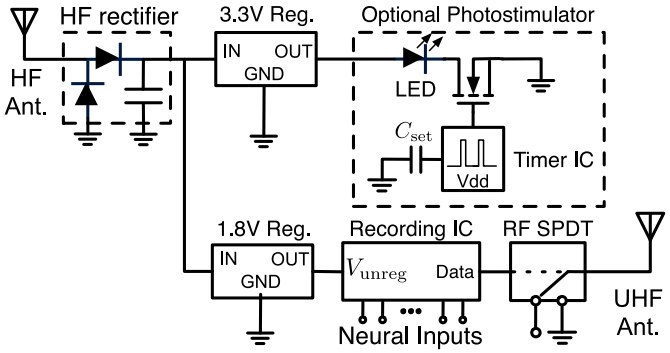

Fig. 2. Implanted device schematic.

system operating at a data rate of 5 Mbps or greater, including an off-the shelf external system, HF WPT, and offering multi-channel neural and electromyography (EMG) recording.

II. Implant Design

A schematic of the envisioned implant is depicted in Fig. 2. A dual-band antenna, described in [15], receives the incoming HF carrier, which is rectified and regulated to provide power to the implant. A previously developed neural/EMG recording integrated circuit (IC) [8] is used to digitize up to a total of 10 neural and 4 EMG inputs. The digital bit stream output from the recording IC drives an SPDT RF switch at the terminals of the UHF antenna to implement BPSK backscatter modulation. Additionally, the capability for optogenetic photostimulation is available via pulse width modulation (PWM) of a blue light emitting diode (LED).

The antenna and the electronic components are encapsulated in a biocompatible silicone polymer (Dow Corning MDX4-4120). The encapsulation procedure uses centrifugation and vacuum curing to remove air bubbles and ensure a tight bond to the circuit. The implant prototype measures 25 mm diameter with a total thickness of 2.8 mm including the substrate, antenna, all circuitry, and biocompatible silicone encapsulation as depicted in Fig. 3.

A. Choice of Operating Frequencies

The 13.56 MHz HF industrial, scientific, and medical (ISM) band was chosen for the WPT application because it provides a high coupling efficiency and low specific absorption rate (SAR) with a relatively small antenna size. The 902−928 MHz UHF ISM band was selected due to the 26 MHz of bandwidth

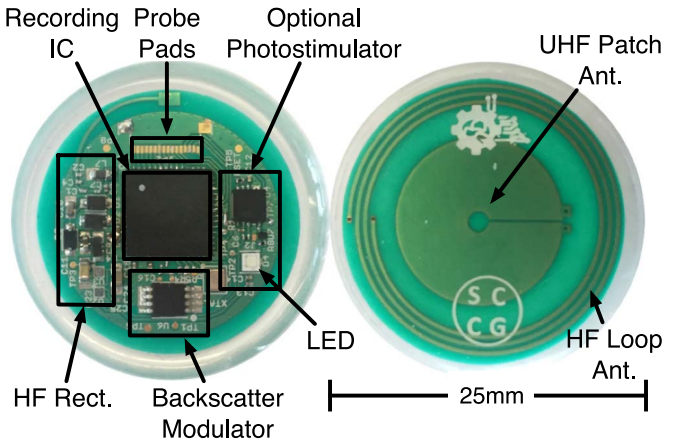

Fig. 3. Implant prototype encapsulated in biocompatible silicone.

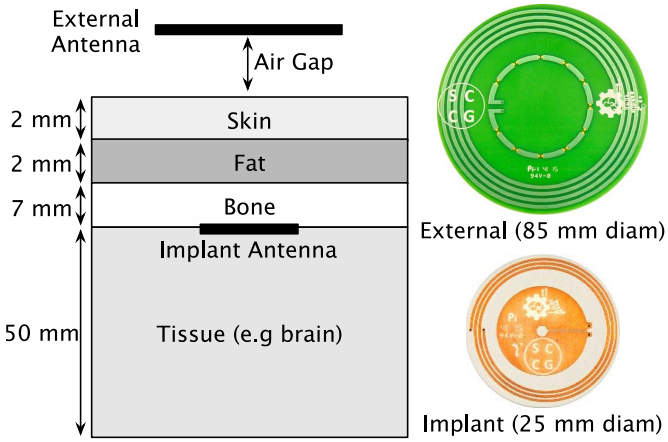

Fig. 4. Implant antenna and layered tissue model used for simulations, from [15].

available and the readily available commercial hardware (e.g., the USRP platform) available in this band.

B. Dual-Band Antenna Subsystem

The implant antenna subsystem was previously described in [15]. In addition to the 25 mm diameter implant antenna, there is an 85 mm diameter external antenna. The antenna system has been previously tested in a saline tissue proxy as well as *in vitro* animal tissue. The antenna structure and the layered tissue model used for full-wave electromagnetic simulation in CST Microwave Studio are depicted in Fig. 4. In a saline tissue proxy, at an implant depth of 11 mm and an air gap of 5 mm, the measured HF power link efficiency is on the order of 17% and the insertion loss of the UHF communication link is on the order of 38 dB.

C. HF Wireless Power Transfer Receiver

A voltage doubling rectifier is used to convert the incoming HF WPT carrier at 13.56 MHz from the external system into direct current (dc) power. The output of the rectifier is regulated using low-dropout (LDO) regulators to provide

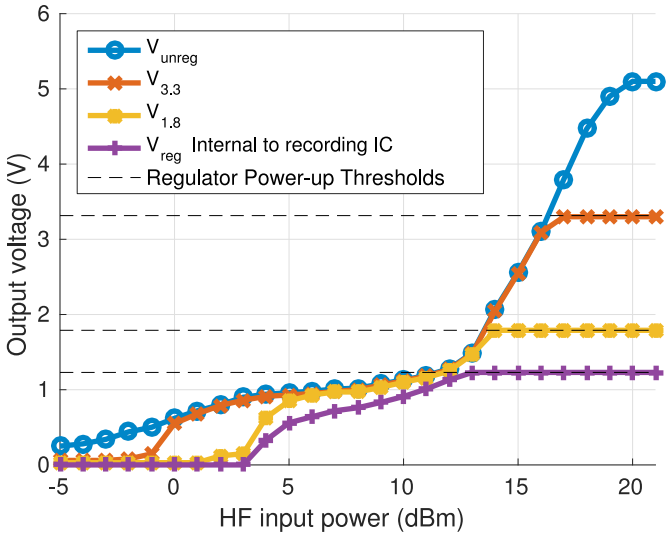

Fig. 5. Regulator outputs vs HF input power. The implant powers-up at an input power of 13 dBm and the optional photostimulator circuit at 17 dBm.

3.3V and 1.8V rails. Significant effort was invested in component selection for small form factor, low power consumption, and over-voltage tolerance. Schottky diodes (1N5711, Diodes Incorporated) were selected due to their high reverse voltage rating of 70 V as well as their low forward voltage drop of 410 mV. Voltage regulators from the Texas Instruments (TI) LP5907 series were selected. A 3.3 V regulator powers the photostimulator and a 1.8 V regulator powers the recording IC. This regulator series was selected due to its package size of only 0.65 x 0.65 mm and low dropout voltage of 120 mV. Most importantly, these regulators have an unusually high measured power supply rejection ratio (PSRR) of approximately 20 dB at 13.56 MHz. This specification is critical in order to reduce the unwanted residual 13.56 MHz ripple coming from the rectifier. For most LDO regulators, the PSRR will be very high at frequencies within the loop bandwidth of the regulator (50 dB or more, for frequencies up to, e.g., 100 kHz), but the PSRR unfortunately decreases to near zero at frequencies of 1 MHz or above. In contrast, the measured high frequency PSRR of the LP5907 series is excellent.

In order to achieve maximum performance from the rectifier, proper matching to the antenna is necessary. The matching component values were calculated with the following procedure: the total dc power consumption of the system was measured and found to be 0.74 mA at 1.8 V (with the photostimulator disabled). A 2432 Ω load was therefore connected to the output of the LDO to emulate the system power consumption. The return loss (|S11|) at the rectifier input (prior to matching) was measured at 13.56 MHz over a range of input powers. The minimum |S11| value was used to calculate the corresponding components for a conjugate match. After matching, the rectifier exhibits 47% efficiency at this operating point. This is very close to the theoretical 50% efficiency that can be achieved with a conjugate match.

The HF WPT system was tested over different input powers in a saline tissue proxy, with 1 cm implant depth and with the external antenna having an air gap of 0.5 cm. Fig. 5 depicts the output of the rectifier and the different board-level and chip-level supply voltages. The HF input power at the external antenna port for which the LDOs enter regulation are as follows:

- Recording IC, integrated 1.23 V LDO: +13 dBm.
- TI 1.8 V LDO: +14 dBm.
- TI 3.3 V LDO: +17 dBm.

Thus a minimum HF drive power of +17 dBm must be supplied under these implant conditions. A 5.1 V Zener diode is integrated into the rectifier circuitry (not shown in Fig. 2) to protect the implant from excess HF power.

III. External System

The commercial off-the-shelf (COTS) external system is depicted in Fig. 6. It is based on an Ettus Research, Inc. USRP B210 which is connected to an added RF front-end that consists of an additional power amplifier and a self-jammer cancellation subsystem.

A. Software Defined Radio Subsystem

The USRP B210 is a low cost ($1100) software defined radio supporting carrier frequencies of $70 - 6000$ MHz, with baseband bandwidth up to 56 MHz. In our system, the USRP B210 is responsible for supplying the UHF communication carrier at 915 MHz and receiving the backscatter subcarriers containing uplink data from the implant. The USRP is connected to a PC with USB 3.0 to control the USRP and convey the baseband data to the PC. GNU Radio, an open source block-based signal processing software was utilized. A custom GNU Radio flowgraph was designed that sets up the USRP hardware at a baseband sampling rate of 20 Msps and processes the incoming I/Q symbols in real-time.

Fig. 7 depicts a simplified view of the proposed GNURadio receiver pipeline. First, a phase locked loop (PLL) that exploits poly-phase filter banks [16] locks to the backscattered symbol frequency and downsamples accordingly. Next, another PLL that exploits the Costas-loop architecture [17] rotates the phase of the symbols onto the in-phase axis so that slicing can be implemented simply by checking the sign of each sample. Then, a bit decision block outputs a string of demodulated bits.

The PC that runs the demodulating software employs 16 GB of RAM and an Intel Core-i7 processor clocked at 3.8 GHz. For rates up to 1.5 Mbps, a Linux pipe can be utilized and the output of the flowgraph can be processed in near-real time from MATLAB using batch processing of 3000 frames at a time. At higher rates, a post-processing approach is used to circumvent the slow speed of MATLAB processing. Fig. 8 depicts an I/Q plot of 10000 samples that were collected after the phase alignment block. The symbols were generated at a rate of 5 Msps using the recording IC and then collected by the USRP-based external system.

The MATLAB script is responsible for post-processing the data generated by the GNU Radio flowgraph. Start-of-frame (SOF) synchronization is performed by correlation with the Barker codes that are embedded in the data stream transmitted by the recording IC [8]. After frame synchronization,

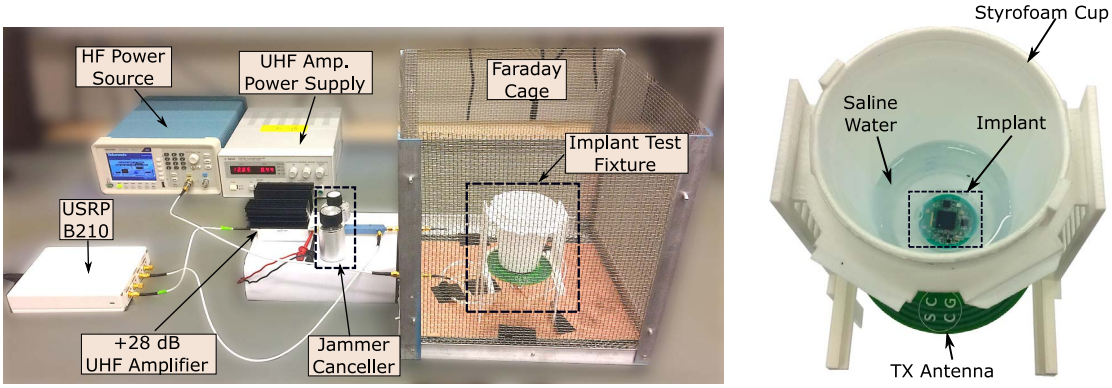

Fig. 6. Left: Implanted communication system testbed. Right: 3D-printed fixture for varying the air-gap and implant depth.

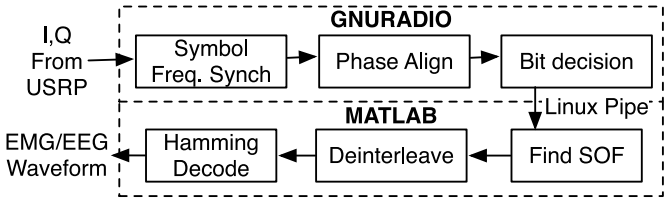

Fig. 7. Proposed receiver pipeline.

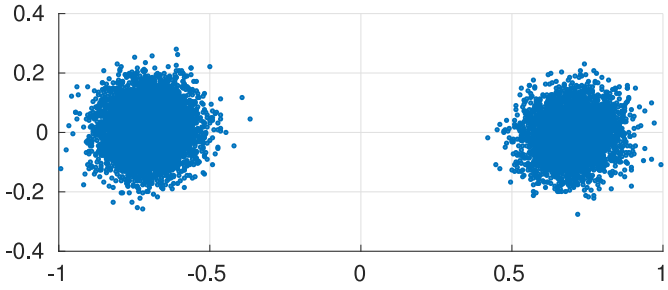

Fig. 8. Measured I/Q samples after the phase-alignment PLL. The samples are synchronized in terms of symbol frequency and rotated in phase onto the in-phase axis.

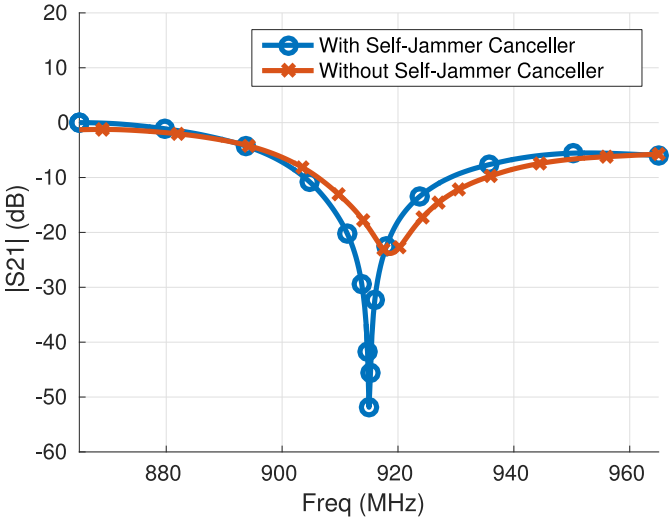

Fig. 9. Measured self-jammer carrier suppression ratio with and without the self-jammer cancellation circuit. The self-jammer canceller reduces the carrier amplitude by $\approx$ 39 dB.

de-interleaving is performed to extract the 16-bit blocks containing the digitized neural/EMG data. The last step is a Hamming (16, 11) decoder that provides single error correction, double error detection (SECDED) functionality to extract the 11-bit neural/EMG samples.

B. RF Interface

A Mini-Circuits ZRL-3500 amplifier increases the carrier power generated by the USRP up to +25 dBm. The output of the amplifier is connected to a self-jammer cancellation circuit as shown in Fig. 1. The latter is comprised of a Mini-Circuits ZX30-20-20BD+ 10 dB directional coupler, a Weinschel 980-2K variable phase shifter (having 100 degrees phase shift range) and a JFW 50R-019 1 dB step attenuator with 0-10 dB attenuation range. With careful adjustment of the phase shifter and the attenuator, the signal that exits the output coupling port contains the backscattered signal with a carrier suppression of up to $\approx$ 39 dB as shown in Fig. 9. Similar directional coupler based self-jammer suppression networks can be found in [18] and [19].

To provide the HF carrier that powers the implant, an Agilent 3350B arbitrary waveform generator (AWG) was utilized. The output HF power at 13.56 MHz can be provided up to +23 dBm, but as previously described, only +17 dBm is required at an 1 cm implant depth, with the external antenna having an air gap of 0.5 cm.

IV. Measurement Results

As shown in Fig. 6, benchtop testing employs a 3D-printed fixture allowing the adjustment of the air gap between the external antenna and the saline tissue proxy (0.91% w/v saline solution). The transmit antenna is placed beneath a styrofoam cup that contains the saline solution, and this fixture is placed in a Faraday cage in order to shield the experiment from external interference.

A. Sensitivity/Range Characterization

To characterize the performance of the backscatter communication link, a benchtop setup with an air gap of 0.5 cm, an

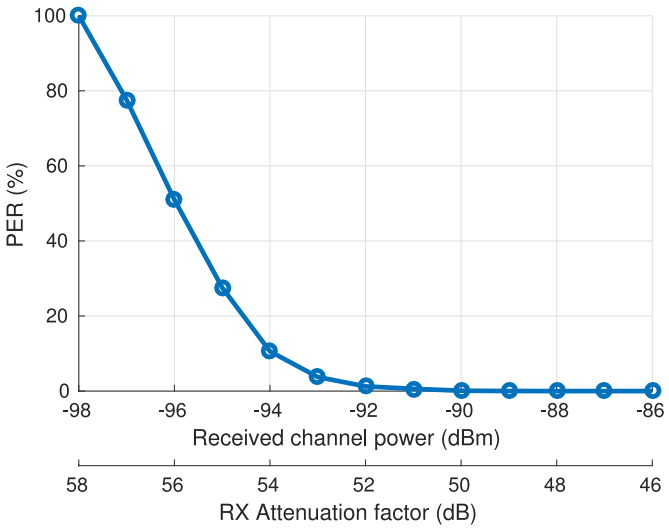

Fig. 10. Packet error rate vs. receive-path attenuation factor and corresponding absolute channel power.

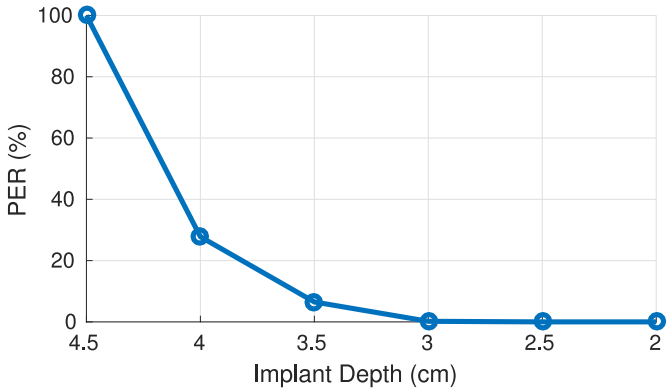

Fig. 11. PER vs implant depth with a fixed UHF carrier power level of 0 dBm.

implant depth of 1 cm and a saline water height of 6 cm was utilized. The in-channel power of the backscattered subcarrier was first measured with a spectrum analyzer at the output-coupled port of the directional coupler. With a +25 dBm carrier power from the external system, the received channel power was measured and found to be −40 dBm under the test conditions.

Variable attenuation in the receive path was used to reduce the available subcarrier power to measure the receive path link margin given the receiver's internally generated noise. Packet error rate (PER) measurements were first made as a function of available channel power by counting cyclic redundancy check (CRC) errors, after Hamming decoding, from 25000 packets for different RX attenuation factors. Fig. 10 depicts the corresponding results. The receiver exhibits a PER of under 0.62 % for an input channel power of −91 dBm.

The system was also characterized for PER as a function of implant depth. In this experiment, the externally supplied carrier power was set to 0 dBm, and the PER was measured using the same method as implant depth was varied, with a fixed air gap of 0.5 cm. Fig. 11 depicts the corresponding results. We observed that the backscatter uplink exhibits a PER of better than 0.19 % at an implant depth of up to 3 cm. Lower carrier power is better for reducing the specific heat absorption rate (SAR) and the system's overall power consumption. Hence, a carrier power of 0 dBm was utilized for this experiment since it yields a sufficient implant depth. It is important to note that time-domain simulations provided a peak UHF SAR value of 0.457 W/kg averaged over 1 g of mass [15]. This peak SAR value is 3.5 times lower than the regulatory limit of 1.6 W/kg.

TABLE I
MEASURED INPUT-REFERRED NOISE LEVELS

	Neural (μV RMS)	EMG (μV RMS)
Implant System - Battery Power	17.8	123.1
Implant System - HF Power	18.9	123.8
IC Alone [8]	5.7	43

B. Measured Frequency Response of Neural/EMG Channels

The neural/EMG recording IC [8] supports up to 10 neural and 4 electromyogram (EMG) channels with a sampling rate of 26.10 kHz for the neural channels and 1.628 kHz for the EMG channels. The EMG and the neural inputs are high-pass filtered at 5 Hz and 250 Hz respectively. Their frequency response was characterized by injecting a sinusoidal test signal at the input. Fig. 13 depicts the measured system response for the neural and EMG inputs.

C. Input-Referred Noise Characterization

The input-referred noise of the entire implant system was characterized, including the recording IC plus wireless power and backscatter communication functions. The noise was quantified by shorting the inputs of the recording IC and measuring the root mean square (RMS) power of the recorded signal, then correcting for the previously measured system gain. To identify any noise contributions from the WPT subsystem, the input referred noise was measured with the implant powered via the HF link and separately when the implant was powered by a battery inside the shielded enclosure.

Table I presents the measured results. The recording IC has a previously measured input-referred noise of 5.7 μV and 43 μV RMS for the neural and the EMG inputs respectively [8]. The increased noise observed in this experiment is due to unwanted parasitic coupling of the UHF data signal into the neural and EMG inputs. We believe this noise elevation can be reduced easily with better attention to PC board layout as well as including a simple R-C low-pass network at the inputs to the recording IC. It can be observed that the HF link introduces less than 2 μV RMS added noise to the system for both EMG and neural inputs.

D. Neural/EMG Measurements

The end-to-end acquisition and telemetry of neural and EMG signals were also characterized using the *in vitro* test setup. Pre-recorded electromyogram (EMG) and neural signals signal were fed into the implant from an Agilent 33500B arbitrary waveform generator (AWG), using an electrode simulator network and a high impedance attenuator.

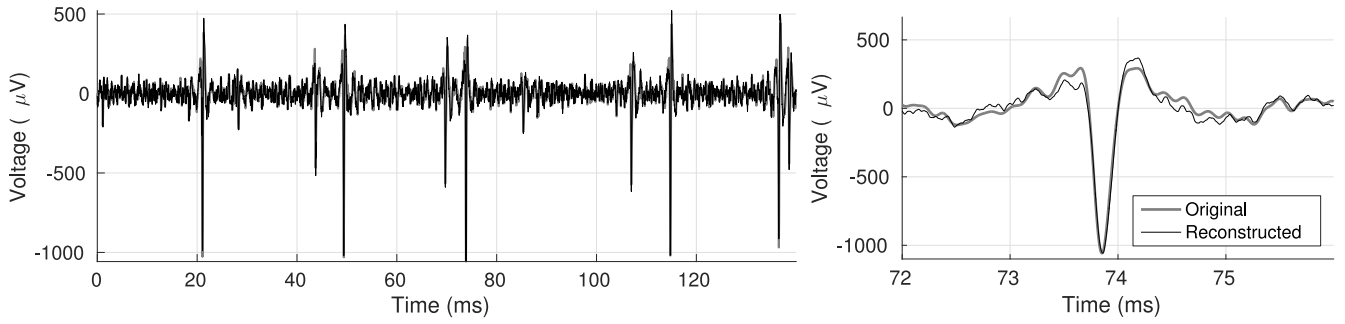

Fig. 12. Original vs. reconstructed neural signal. Left: complete reconstructed and original waveforms. Right: zoomed-in depiction of one of the spikes that occur at approx. 74 ms.

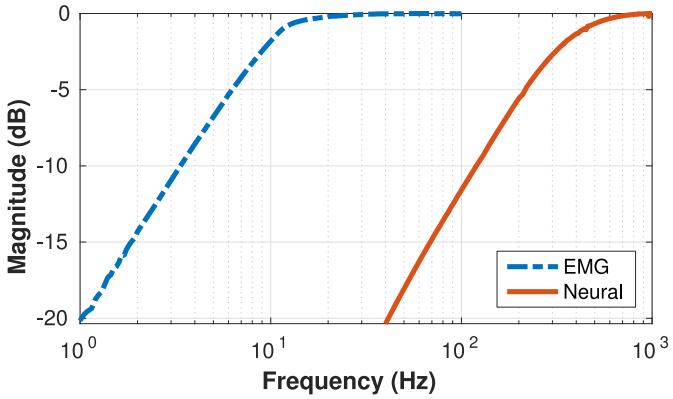

Fig. 13. Measured frequency response of neural and EMG inputs.

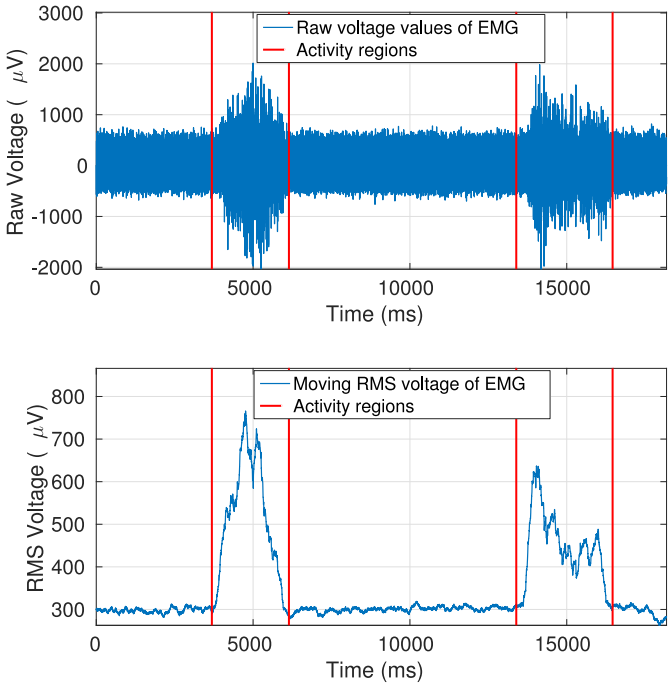

Fig. 14. Measurements of the bicep brachii muscle activity on a human subject using one of the proposed system's EMG channels. Top: Raw EMG voltage values. Bottom: Post-processed data using a moving RMS filter with a window duration of 300 ms.

Testing of the neural inputs used prerecorded neural signals that were acquired from the motor cortex of a non-human primate by our colleagues under an IACUC approved protocol. A total of 130 ms of data were captured from the forearm area of left primary motor cortex of the monkey Macaca nemestrina. The monkey was implanted with a Utah microelectrode array [20] and the signals were captured and digitized with the Neurochip platform [21] at a sampling rate of 21 kHz. This pre-recorded signal was filtered with a passband of 500-7000 Hz and loaded into the AWG for subsequent playback.

The proposed system was set up with the receiver recording in real time and the implant powered by HF wireless power. An implant depth of 1 cm and an air gap of 0.5 cm were used. The comparison between the pre-recorded signal and the signal obtained from the proposed system are depicted in Fig. 12. On the left side of the figure, the time domain representation of the entire 130 ms of data is plotted, while on the right a zoomed-in view depicts a single spike. Excellent agreement is observed between the two waveforms.

Lastly, the capability of the proposed system for detecting muscle activity was tested. For this experiment,the terminals of one of the EMG amplifier inputs were connected to commodity EMG electrodes. The electrodes were placed in adjacent positions on the left bicep brachii area of a human subject. Moreover, a reference electrode was placed below the wrist flexor of the subject and connected to the implant's ground. The proposed system was powered over the HF link and the receiver was set up to demodulate data in real-time for a total of 18 seconds. After initiating the recording the subject was instructed to contract their muscles for 1 second at time intervals of 4 and 14 seconds.

The corresponding results are depicted in Fig. 14. The time periods during which the subject contracted their muscles are designated with vertical red lines. The top part of the figure depicts the raw EMG voltage values. Spikes with amplitudes of up to 4 mVpp can be observed during the periods of muscle activity. EMG signals are typically processed using a moving RMS filter [22] in order to reduce high frequency noise and smooth the inherently spiked data. The bottom part of Fig. 14 shows the result of a moving RMS filter with a window duration of 300 ms that was applied on the raw data. Especially after filtering, muscle activity can be identified with excellent clarity.

V. Conclusion

This paper presents a dual-band approach for HF wireless power delivery and UHF backscatter communication in implanted biomedical devices. A testbed is presented including a custom implanted device as well as an external system based on a commercially available USRP B210 software defined radio (SDR) platform. The implant integrates a BPSK backscatter uplink rate of 5 Mbps, with an HF WPT link delivering 1.33 mW at an efficiency of 47%. The implant is 25 mm in diameter and 2.8 mm thick, including the printed circuit substrate, dual-band antenna, all circuitry, and biocompatible silicone encapsulation. It supports up to 10 neural and 4 electromyogram (EMG) channels with a sampling rate of 26.10 kHz for the neural channels and 1.628 kHz for the EMG channels. The communication link is shown to have 0% packet error rate at an implant depth of up to 2.5 cm.

Future work includes noise mitigation via a revised PC board layout as well as including a simple R-C low-pass network at the inputs to the recording IC to reduce unwanted parasitic coupling between the UHF data signal and the neural and EMG inputs. Further *in vitro* testing will be conducted to ensure both neural and EMG recording performance before commencing *in vivo* work with animals such as rodents and non-human primates. Additional work includes development of higher communication rate implants by exploiting higher order backscatter, such as QAM modulated backscatter [23].

Acknowledgment

The content is solely the responsibility of the authors and does not necessarily represent the official views of the National Science Foundation. The authors would also like to thank Prof. Eberhard E. Fetz and Mr. Andrew Bogaard for providing the pre-recorded neural signals.

References

[1] N. Bhadra and K. L. Kilgore, "High-frequency electrical conduction block of mammalian peripheral motor nerve," *Muscle Nerve*, vol. 32, no. 6, pp. 782–790, 2005.
[2] K. Birmingham *et al.*, "Bioelectronic medicines: A research roadmap," *Nat. Rev. Drug Disc.*, vol. 13, no. 6, pp. 399–400, 2014.
[3] M. M. Maharbiz, R. Muller, E. Alon, J. M. Rabaey, and J. M. Carmena, "Reliable next-generation cortical interfaces for chronic brain-machine interfaces and neuroscience," *Proc. IEEE*, vol. 105, no. 1, pp. 73–82, Jan. 2017.
[4] N. M. Neihart and R. R. Harrison, "Micropower circuits for bidirectional wireless telemetry in neural recording applications," *IEEE Trans. Biomed. Eng.*, vol. 52, no. 11, pp. 1950–1959, Nov. 2005.
[5] P. Ledochowitsch, A. C. Koralek, D. Moses, J. M. Carmena, and M. M. Maharbiz, "Sub-mm functional decoupling of electrocortical signals through closed-loop BMI learning," in *Proc. IEEE Eng. Med. Biol.*, Jul. 2013, pp. 5622–5625.
[6] S. Ha *et al.*, "Silicon-integrated high-density electrocortical interfaces," *Proc. IEEE*, vol. 105, no. 1, pp. 11–33, Jan. 2017.
[7] J. S. Besnoff and M. S. Reynolds, "Near field modulated backscatter for in vivo biotelemetry," in *Proc. IEEE Int. Conf. RFID (RFID)*, Orlando, FL, USA, Apr. 2012, pp. 135–140.
[8] S. J. Thomas, R. R. Harrison, A. Leonardo, and M. S. Reynolds, "A battery-free multichannel digital neural/EMG telemetry system for flying insects," *IEEE Trans. Biomed. Circuits Syst.*, vol. 6, no. 5, pp. 424–436, Oct. 2012.
[9] J. Charthad, M. J. Weber, T. C. Chang, and A. Arbabian, "A mm-sized implantable medical device (IMD) with ultrasonic power transfer and a hybrid bi-directional data link," *IEEE J. Solid-State Circuits*, vol. 50, no. 8, pp. 1741–1753, Aug. 2015.
[10] D. Seo *et al.*, "Wireless recording in the peripheral nervous system with ultrasonic neural dust," *Neuron*, vol. 91, no. 3, pp. 529–539, 2016.
[11] H. Ando *et al.*, "Wireless multichannel neural recording with a 128-Mbps UWB transmitter for an implantable brain-machine interfaces," *IEEE Trans. Biomed. Circuits Syst.*, vol. 10, no. 6, pp. 1068–1078, Dec. 2016.
[12] A. P. Sample, D. T. Meyer, and J. R. Smith, "Analysis, experimental results, and range adaptation of magnetically coupled resonators for wireless power transfer," *IEEE Trans. Ind. Electron*, vol. 58, no. 2, pp. 544–554, Feb. 2011.
[13] X. Li, C.-Y. Tsui, and W.-H. Ki, "A 13.56 MHz wireless power transfer system with reconfigurable resonant regulating rectifier and wireless power control for implantable medical devices," *IEEE J. Solid-State Circuits*, vol. 50, no. 4, pp. 978–989, Apr. 2015.
[14] R. Muller *et al.*, "A minimally invasive 64-channel wireless μECoG implant," *IEEE J. Solid-State Circuits*, vol. 50, no. 1, pp. 344–359, Jan. 2015.
[15] A. Sharma, E. Kampianakis, and M. S. Reynolds, "A dual-band HF and UHF antenna system for implanted neural recording and stimulation devices," *IEEE Antennas Wireless Propag. Lett.*, vol. 16, pp. 493–496, 2016.
[16] T. W. Rondeau, V. Shelburne, and V. O'Shea, "Designing anaylsis and synthesis filterbanks in GNU radio," in *Proc. Karlsruhe Workshop Softw. Radios*, Mar. 2014, pp. 20–29.
[17] J. P. Costas, "Synchronous communications," *Proc. IRE*, vol. 44, no. 12, pp. 1713–1718, Dec. 1956.
[18] J. C. Carrick *et al.*, "Methods and apparatus for self-jamming suppression in a radio frequency identification (RFID) reader," U.S. Patent 20 100 069 011, Mar. 18, 2010.
[19] J.-Y. Jung, C.-W. Park, and K.-W. Yeom, "A novel carrier leakage suppression front-end for UHF RFID reader," *IEEE Trans. Microw. Theory Techn.*, vol. 60, no. 5, pp. 1468–1477, May 2012.
[20] E. M. Maynard, C. T. Nordhausen, and R. A. Normann, "The utah intracortical electrode array: A recording structure for potential brain-computer interfaces," *Electroencephalography Clin. Neurophysiol.*, vol. 102, no. 3, pp. 228–239, 1997.
[21] S. Zanos, A. G. Richardson, L. Shupe, F. P. Miles, and E. E. Fetz, "The Neurochip-2: An autonomous head-fixed computer for recording and stimulating in freely behaving monkeys," *IEEE Trans. Neural Syst. Rehabil. Eng.*, vol. 19, no. 4, pp. 427–435, Aug. 2011.
[22] R. Merletti, "Standards for reporting EMG data," *J. Electromyography Kinesiol.*, vol. 9, no. 1, pp. 3–4, 1999.
[23] S. J. Thomas, E. Wheeler, J. Teizer, and M. S. Reynolds, "Quadrature amplitude modulated backscatter in passive and semipassive UHF RFID systems," *IEEE Trans. Microw. Theory Techn.*, vol. 60, no. 4, pp. 1175–1182, Apr. 2012.

Eleftherios Kampianakis (S'15) received the B.S. and M.S. degrees in electronic and computer engineering from the Technical University of Crete, Greece. He was a recipient of the Best Diploma Thesis Award on the pan-hellenic IEEE VTS & AESS Joint Greece Chapter Final/Diploma Thesis Competition for the years 2009–2011 for his Diploma thesis on over-the-air programmable wireless sensor networks (WSN) and one of the best papers at the IEEE SENSORS Conference 2013. He developed a low-cost and low-power WSN for environmental sensing exploiting backscatter communication principles.

He is currently pursuing the Ph.D. degree with the Department of Electrical Engineering, University of Washington, Seattle, WA, USA. His research interests include backscatter communication and implantable biomedical devices.

Apoorva Sharma (S'15) received the B.Tech. degree in electronics and communication engineering from the Galgotias College of Engineering and Technology, India, in 2009 and the M.Sc. (tech.) degree from the International Institute of Information Technology Hyderabad, India, in 2011.

She is currently pursuing the Ph.D. degree with the Department of Electrical Engineering, University of Washington, Seattle, WA, USA. From 2011 to 2013, she was with Computer Simulation Technology India, where she held the position of Application Engineer and was responsible for technical support and benchmarks for CST Microwave Studio, Cable Studio, Particle Studio and Design Studio software. She also helped in improving the database of Antenna Magus. Her research interests include modeling and optimization techniques of RF devices, electromagnetics, antenna designs, and implantable devices.

José Arenas received the B.S. and M.S. degrees in mechanical engineering from the Pontificia Universidad Catlica de Chile, Santiago, Chile, in 2008 and 2011, respectively, and the M.S. degree in electrical engineering from the University of Washington, Seattle, WA, USA, in 2017. He participated in UW EE's Sensing Computing Communications Group as a Project Collaborator and was involved in applications regarding microwave imaging and implantable devices. His research interests include the development of small form factor embedded systems with wireless links for both industrial and mass consumer use.

He is currently with Nytec Inc. as part of a multidiscipline team designing consumer electronics products.

Matthew S. Reynolds (S'01–M'02–SM'10) received the S.B., M.Eng., and Ph.D. degrees from the Massachusetts Institute of Technology, Cambridge, MA, USA, in 1998, 1999, and 2003, respectively.

He is currently an Associate Professor of electrical engineering and computer science and engineering with the University of Washington, Seattle, WA, USA. He is a Co-Founder of the RFID systems firm, ThingMagic Inc., the demand-side energy conservation technology firm Zensi, and the home sensing company SNUPI Inc. His research interests include the physics of sensors and actuators, RF identification, microwave and millimeter wave imaging, and sensor signal processing.